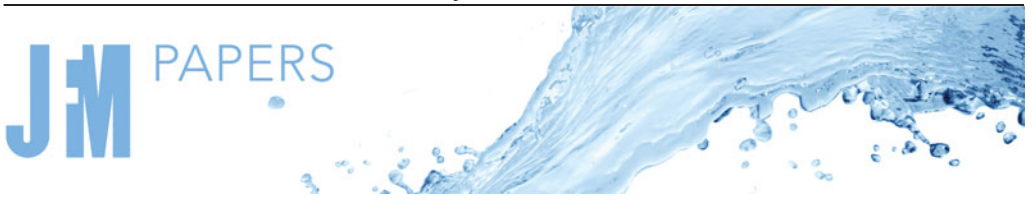
J. Fluid Mech. (2021), *vol*. 913, A15, doi:10.1017/jfm.2020.1157



Density and surface tension effects on vortex stability. Part 2. Moore–Saffman–Tsai–Widnall instability

Ching Chang[1],† **and Stefan G. Llewellyn Smith**[1,2]

[1]Department of Mechanical and Aerospace Engineering, Jacobs School of Engineering, UCSD, 9500 Gilman Drive, La Jolla, CA 92093-0411, USA

[2]Scripps Institution of Oceanography, UCSD, 9500 Gilman Drive, La Jolla, CA 92093-0213, USA

(Received 6 August 2020; revised 21 November 2020; accepted 16 December 2020)

The Moore–Saffman–Tsai–Widnall (MSTW) instability is a parametric instability that arises in strained vortex columns. The strain is assumed to be weak and perpendicular to the vortex axis. In this second part of our investigation of vortex instability including density and surface tension effects, a linear stability analysis for this situation is presented. The instability is caused by resonance between two Kelvin waves with azimuthal wavenumber separated by two. The dispersion relation for Kelvin waves and resonant modes are obtained. Results show that the stationary resonant waves for $m = \pm 1$ are more unstable when the density ratio ρ_2/ρ_1, the ratio of vortex to ambient fluid density, approaches zero, whereas the growth rate is maximised near $\rho_2/\rho_1 = 0.215$ for the resonance $(m, m+2) = (0, 2)$. Surface tension suppresses the instability, but its effect is less significant than that of density. As the azimuthal wavenumber m increases, the MSTW instability decays, in contrast to the curvature instability examined in Part 1 (Chang & Llewellyn Smith, *J. Fluid Mech.* vol. 913, 2021, A14).

Key words: parametric instability, vortex instability

1. Introduction

This paper is the second part of a study on the effects of density and surface tension on parametric vortex stability. A possible mechanism of instability was proposed by Widnall, Bliss & Tsai (1974) in their study of vortex ring stability. These authors argued that a basic state solution subject to neutrally stable disturbances $\tilde{u}$ of $O(\delta)$, $\delta \ll 1$, can be unstable with the addition of a physical effect represented by a small parameter. The solution is then expanded as a perturbation series in orders of the parameter, setting the stage for possible

† Email address for correspondence: chc054@eng.ucsd.edu

© The Author(s), 2021. Published by Cambridge University Press

https://doi.org/10.1017/jfm.2020.1157 Published online by Cambridge University Press

resonance between two neutrally stable $O(\delta)$ modes. The resonant instability appears as a consequence at order δ multiplied by the small parameter and is called parametric instability.

Two types of parametric instabilities have been discovered for vortices: the Moore–Saffman–Tsai–Widnall (MSTW) instability and the curvature instability. The MSTW instability was first discovered by Moore & Saffman (1975) and Tsai & Widnall (1976), and has since been revisited by Fukumoto (2003) among others. The basic state is a vortex column with uniform vorticity inside the column and zero outside the column. It is, hence, a Rankine vortex that extends uniformly in the third dimension. Linear analysis shows that the $O(1)$ vortex column is neutrally stable when disturbed by waves of $O(\delta)$. Those $O(\delta)$ disturbances are Kelvin waves. Motivated by the goal of examining vortex ring stability, weak strain, measured by the small parameter γ. This situation leads to the MSTW instability, which is the focus of the present work. This is an approximation to the vortex ring case with no basic-state curvature, but with the leading-order strain retained. In the curvature instability studied in Chang & Llewellyn Smith (2021), hereafter Part 1 of this work, the basic state is expanded in terms of the ratio of the core size of the vortex ring to its radius of curvature, ϵ, and is curved at $O(\epsilon)$. Moore & Saffman (1975) and Tsai & Widnall (1976) found that when a weak strain field is imposed on the vortex, perpendicular to its axis, an instability emerges due to the strain field. The strain field is mathematically a quadrupole, and enables a resonance between two Kelvin waves of azimuthal wavenumber m and $m+2$. The MSTW instability has been studied extensively since then (e.g. Éloy & Le Dizès 2001; Fukumoto 2003). In the short-wavelength regime, it has been shown to be the elliptic instability of Bayly (1986), Waleffe (1990) and Leweke & Williamson (1998). Blanco-Rodriguez & Le Dizès (2016) theoretically studied the short-wave elliptic instability of a Batchelor vortex (a Gaussian core). A recent study using direct numerical simulations (DNS) by Hattori, Blanco-Rodriguez & Le Dizès (2019) showed that both types of parametric instabilities exist in the short-wavelength regime, and that the elliptic instability dominates over the curvature instability.

The stability of a strained vortex column was also investigated in the context of aircraft trailing vortices. The mutual interaction between long waves causes the Crow instability (Crow 1970). The Biot–Savart law is used to compute the induced velocity on one of the trailing vortices owing to the presence of the other. In a frame fixed to one of the vortices, a weak strain field is created by the other vortex in the thin-core limit providing their separation is large. Moore & Saffman (1971) obtained a solution represented as a perturbation series in γ, where $\gamma \ll 1$ is the strength of the strain field. The core boundary deforms into an elliptic shape at $O(\gamma)$:

$$F = 1 + \tfrac{1}{2}\gamma \cos 2\theta + O(\gamma^2). \tag{1.1}$$

The stability of the strained vortex was also investigated by Moore & Saffman (1971) for two- and three-dimensional long-wave disturbances. Moore & Saffman (1975) and Tsai & Widnall (1976) studied the instability mechanism proposed by Widnall *et al.* (1974) for short-wave disturbances. Fukumoto (2003) extended the stability calculation for intersection points of Kelvin wave dispersion curves.

Historically, the curvature instability (Hattori & Fukumoto 2003; Fukumoto & Hattori 2005) was discovered later than the MSTW instability. We have examined it in the presence of density and surface tension effects in Part 1 of this study (Chang & Llewellyn Smith 2021). In the asymptotic analysis by Fukumoto & Hattori (2005), the authors argued that the curvature instability dominates over the MSTW instability provided that $\epsilon \ll 1$. However, in the recent numerical simulations by Hattori *et al.* (2019), the elliptic instability

https://doi.org/10.1017/jfm.2020.1157 Published online by Cambridge University Press

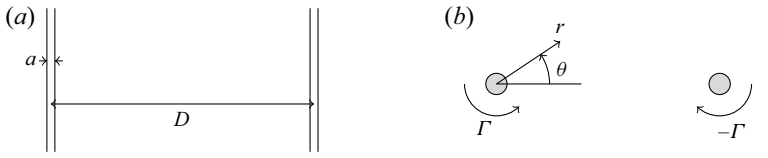


Figure 1. (*a*) Side view of two parallel vortex tubes and (*b*) a cross-section view of the counter-rotating vortices. The shaded areas are occupied by fluid of density ρ_2, whereas the ambient density is ρ_1.

(short-wavelength MSTW) is found to be dominant for a vortex ring with or without swirl, and the curvature instability is only detected when swirl is present. As shown in the study by Blanco-Rodriguez & Le Dizès (2016), the MSTW instability can be applied to different configurations such as a single vortex ring, an array of rings and vortex helix. Here we just do not consider such generalisations and treat the simplest case of two parallel counter-rotating vortices.

The effect of density (or stratification) on vortex instability has been in examined by Joly, Fontane & Chassaing (2005), Sipp *et al.* (2005), Dixit & Govindarajan (2011), Saunders (1973), among others (see also the references therein). However, the effect of density on the MSTW instability has not been investigated previously. In the present paper, we follow the formulation in Tsai & Widnall (1976) and Fukumoto (2003) but include density and surface tension. In § 2, the mathematical formulation including governing equations, boundary conditions and the basic state solution are given. Linearised equations at $O(\delta)$ and $O(\delta\epsilon)$ are also derived. The solutions at both orders with density and surface tension are discussed in § 3. We shown results for stationary resonance between $(m, m+2) = (-1, 1)$ in § 4, followed by resonance for $m \geqslant 0$ in § 5. We conclude in § 6.

2. Formulation

Two thin parallel vortex tubes are considered, as shown in figure 1(*a*). We assume that $\gamma = a/D \ll 1$, where a is the core size and R is the separation between two vortices. The outer region and the vortical cores have constant densities ρ_1 and ρ_2, respectively. The circulation of the core is Γ for both vortices but with opposite sign. We normalise the problem by length scale a, velocity scale $U_c = \Gamma/(2\pi a)$ and time scale $2\pi a^2/\Gamma$, whereas the pressure scale is taken to be $\rho_2(\Gamma/2\pi a)^2$. The velocity potential describing the outer irrotational flow is scaled by $\Gamma/2\pi$.

Each vortex tube experiences a strain field perpendicular to its centreline owing to the other vortex tube. The strain is a quadrupole field of strength $O(\gamma)$. We focus on the vortex on the left (see figure 1*b*). This model can be seen as an approximation for a vortex ring, with γ representing the local effect of the strain from the induced motion due to the rest of the vortex ring. We neglect terms of $O(\gamma^2)$ and higher in the following formulation.

2.1. *Governing equations*

We use cylindrical coordinates (r, θ, z), with velocity $\boldsymbol{u} = (u, v, w)$. The undisturbed core boundary is taken to be $r = 1$. As the core is rotational, the governing equations for an inviscid, incompressible flow are the Euler equations inside the core,

$$\nabla \cdot \boldsymbol{u} = 0, \quad \frac{\partial \boldsymbol{u}}{\partial t} + \boldsymbol{u} \cdot \nabla \boldsymbol{u} = -\nabla p. \tag{2.1a,b}$$

https://doi.org/10.1017/jfm.2020.1157 Published online by Cambridge University Press

Vorticity is zero outside the core of the vortex ring, and the Laplace equation governing the velocity potential in this irrotational region is

$$\nabla^2 \Phi = 0. \tag{2.2}$$

In cylindrical coordinates the Euler equations are

$$\frac{\partial u}{\partial t} + \boldsymbol{u} \cdot \nabla u - \frac{v^2}{r} = -\frac{\partial p}{\partial r}, \tag{2.3}$$

$$\frac{\partial v}{\partial t} + \boldsymbol{u} \cdot \nabla v + \frac{uv}{r} = -\frac{1}{r}\frac{\partial p}{\partial \theta}, \tag{2.4}$$

$$\frac{\partial w}{\partial t} + \boldsymbol{u} \cdot \nabla w = -\frac{\partial p}{\partial z}, \tag{2.5}$$

where

$$\boldsymbol{u} \cdot \nabla = u\frac{\partial}{\partial r} + \frac{v}{r}\frac{\partial}{\partial \theta} + w\frac{\partial}{\partial z}. \tag{2.6}$$

The continuity equation is

$$\frac{1}{r}\frac{\partial}{\partial r}(ru) + \frac{1}{r}\frac{\partial v}{\partial \theta} + \frac{\partial w}{\partial z} = 0. \tag{2.7}$$

Outside the core, Laplace's equation is

$$\frac{1}{r}\frac{\partial}{\partial r}\left(r\frac{\partial \Phi}{\partial r}\right) + \frac{1}{r^2}\frac{\partial^2 \Phi}{\partial \theta^2} + \frac{\partial^2 \Phi}{\partial z^2} = 0. \tag{2.8}$$

The solution to (2.3) and (2.7) is called the inner solution, whereas the outer solution refers to the solution of (2.8).

2.2. *Boundary conditions*

The boundary of the vortex is taken to be $r = F$, where $F(\theta; \gamma)$ will be obtained as part of the solution. The inner and outer solutions are matched on the core boundary where $r = F$. For inviscid flows, the matching is given by the kinematic and the dynamic conditions. The kinematic condition gives

$$\frac{\mathrm{D}}{\mathrm{D}t}(r - F)\bigg|_{r=F^-} = \frac{\mathrm{D}}{\mathrm{D}t}(r - F)\bigg|_{r=F^+} = 0, \tag{2.9}$$

where $\mathrm{D}/\mathrm{D}t = \partial/\partial t + \boldsymbol{u} \cdot \nabla$ is the Lagrangian time derivative.

The dynamic condition requires pressure to be continuous without surface tension or to have a jump given by surface tension. In terms of the inner pressure p and outer velocity potential Φ, this becomes

$$\frac{\rho_2}{\rho_1}p + \frac{\partial \Phi}{\partial t} + \frac{1}{2}|\nabla \Phi|^2 = S\nabla \cdot \boldsymbol{n}. \tag{2.10}$$

Here S is dimensionless surface tension $\sigma/[\rho_1 a(\Gamma/2\pi a)^2]$ and $\boldsymbol{n} = \nabla(r - F)/|\nabla(r - F)|$ is the outward normal vector on the boundary.

https://doi.org/10.1017/jfm.2020.1157 Published online by Cambridge University Press

2.3. *The mean-flow solution*

The solution to (2.3)–(2.8) (written using uppercase letters) can be obtained as a perturbation series in γ:

$$\boldsymbol{U} = \boldsymbol{U}_0 + \gamma \boldsymbol{U}_1 + \cdots, \quad P = P_0 + \gamma P_1 + \cdots, \quad \Phi = \Phi_0 + \gamma \Phi_1 + \cdots, \tag{2.11a–c}$$

where γ is the strength of the strain field.

The leading-order mean-flow solution is the Rankine vortex with velocity and pressure fields

$$(U_0, V_0, W_0) = (0, r, 0), \quad P_0 = \frac{1}{2}\left(r^2 - 1 - \frac{\rho_1}{\rho_2}\right) + \frac{\rho_1}{\rho_2} S \tag{2.12a,b}$$

and

$$\Phi_0 = \theta. \tag{2.13}$$

The strain field leads to the following $O(\gamma)$ solution of the mean flow (cf. the solution in Moore & Saffman 1971):

$$U_1 = -r \sin 2\theta, \quad V_1 = -r \cos 2\theta, \quad P_1 = 0 \tag{2.14a–c}$$

in the inner region, whereas the outer solution is

$$\Phi_1 = \frac{1}{8}\left[\frac{3}{r^2} - r^2 - \frac{\rho_2}{\rho_1}\left(\frac{1}{r^2} + r^2\right) + 3S\left(\frac{1}{r^2} + r^2\right)\right] \sin 2\theta. \tag{2.15}$$

The shape of the boundary to $O(\gamma)$ is

$$F(\theta; \gamma) = F_0 + \gamma F_1 + \cdots = 1 + \gamma \frac{1}{2} \cos 2\theta + O(\gamma^2). \tag{2.16}$$

See appendix A for the detailed calculations leading to (2.12*a*,*b*)–(2.16).

2.4. *Linearised equations and boundary conditions for infinitesimal disturbances*

We disturb the mean flow derived in § 2.3 as follows:

$$U + \tilde{u}, \quad V + \tilde{v}, \quad W + \tilde{w}, \quad P + \tilde{p}, \quad \Phi + \tilde{\phi}, \tag{2.17a–e}$$

and the disturbed boundary is $r = F + \tilde{f}$. We use tildes over lowercase letters to represent the disturbances. Disturbances are assumed to be of $O(\delta)$ compared with the $O(1)$ basic state with $\delta \ll 1$. The usual stability analysis treats $O(\delta)$ disturbances. Here, these are neutrally stable as shown in § 3.1, and it is the $O(\delta\gamma)$ solution that is of interest for parametric instability. The disturbances are decomposed into normal modes in the axial direction z and time t. As with the basic solution, disturbances are expanded in γ as

$$\tilde{\boldsymbol{u}} = (\tilde{\boldsymbol{u}}_0 + \gamma \tilde{\boldsymbol{u}}_1 + \cdots) \exp(\mathrm{i}(kz - \omega t)), \tag{2.18}$$

$$\tilde{p} = (\tilde{p}_0 + \gamma \tilde{p}_1 + \cdots) \exp(\mathrm{i}(kz - \omega t)), \tag{2.19}$$

$$\tilde{\phi} = (\tilde{\phi}_0 + \gamma \tilde{\phi}_1 + \cdots) \exp(\mathrm{i}(kz - \omega t)). \tag{2.20}$$

The axial wavenumber and the frequency are also expanded as

$$k = k_0 + \gamma k_1 + \cdots, \quad \omega = \omega_0 + \gamma \omega_1 + \cdots. \tag{2.21a,b}$$

The core boundary disturbance is

$$\tilde{f} = (\tilde{f}_0 + \gamma \tilde{f}_1 + \cdots) \exp(\mathrm{i}(kz - \omega t)). \tag{2.22}$$

As the disturbances $(\tilde{\boldsymbol{u}}, \tilde{p}, \tilde{\phi})$ are small compared with the basic solution $(\boldsymbol{U}, P, \Phi)$, (2.3)–(2.8) can investigated at $O(\delta)$ and $O(\delta\gamma)$ in what follows.

https://doi.org/10.1017/jfm.2020.1157 Published online by Cambridge University Press

2.4.1. *$O(\delta)$ linearised equations and boundary conditions*
The linearised equations for disturbances at $O(\delta)$ are

$$-\mathrm{i}\omega_0\tilde{u}_0 + \frac{V_0}{r}\frac{\partial\tilde{u}_0}{\partial\theta} - \frac{2V_0\tilde{v}_0}{r} = -\frac{\partial\tilde{p}_0}{\partial r}, \tag{2.23}$$

$$-\mathrm{i}\omega_0\tilde{v}_0 + \tilde{u}_0\frac{\partial V_0}{\partial r} + \frac{V_0}{r}\frac{\partial\tilde{v}_0}{\partial\theta} + \frac{V_0\tilde{u}_0}{r} = -\frac{1}{r}\frac{\partial\tilde{p}_0}{\partial\theta}, \tag{2.24}$$

$$-\mathrm{i}\omega_0\tilde{w}_0 + \frac{V_0}{r}\frac{\partial\tilde{w}_0}{\partial\theta} = -\mathrm{i}k_0\tilde{p}_0, \tag{2.25}$$

$$\frac{1}{r}\frac{\partial}{\partial r}(r\tilde{u}_0) + \frac{1}{r}\frac{\partial\tilde{v}_0}{\partial\theta} + \mathrm{i}k_0\tilde{w}_0 = 0 \tag{2.26}$$

for the inside and

$$\frac{1}{r}\frac{\partial}{\partial r}\left(r\frac{\partial\tilde{\phi}_0}{\partial r}\right) + \frac{1}{r^2}\frac{\partial^2\tilde{\phi}_0}{\partial\theta^2} - k_0^2\tilde{\phi}_0 = 0 \tag{2.27}$$

for the outside. The linearised boundary conditions at $r = 1$ are

$$-\mathrm{i}\omega_0\tilde{f}_0 + \frac{\partial\tilde{f}_0}{\partial\theta} = \tilde{u}_0, \tag{2.28}$$

$$\tilde{u}_0 = \frac{\partial\tilde{\phi}_0}{\partial r}, \tag{2.29}$$

$$\frac{\rho_2}{\rho_1}\tilde{p}_0 - \mathrm{i}\omega_0\tilde{\phi}_0 + \frac{\partial\tilde{\phi}_0}{\partial\theta} = \left(1 - \frac{\rho_2}{\rho_1}\right)\tilde{f}_0 - S\left(\frac{\partial^2\tilde{f}_0}{\partial\theta^2} - k_0^2\tilde{f}_0\right). \tag{2.30}$$

The solutions are Kelvin waves given in appendix B.

2.4.2. *$O(\delta\gamma)$ linearised equations and boundary conditions*
We proceed to the next order in the expansion in γ. The equations for disturbances of $O(\delta\gamma)$ are also linearised. The inner solution satisfies

$$\begin{aligned}&-\mathrm{i}\omega_0\tilde{u}_1 + \frac{\partial\tilde{u}_1}{\partial\theta} - 2\tilde{v}_1 + \frac{\partial\tilde{p}_1}{\partial r}\\ &\quad= \left(\mathrm{i}\omega_1 - \frac{\partial U_1}{\partial r}\right)\tilde{u}_0 - U_1\frac{\partial\tilde{u}_0}{\partial r} - \frac{V_1}{r}\frac{\partial\tilde{u}_0}{\partial\theta} - \left(\frac{1}{r}\frac{\partial U_1}{\partial\theta} - \frac{2V_1}{r}\right)\tilde{v}_0,\end{aligned} \tag{2.31}$$

$$\begin{aligned}&-\mathrm{i}\omega_0\tilde{v}_1 + 2\tilde{u}_1 + \frac{\partial\tilde{v}_1}{\partial\theta} + \frac{1}{r}\frac{\partial\tilde{p}_1}{\partial\theta}\\ &\quad= \left(\mathrm{i}\omega_1 - \frac{1}{r}\frac{\partial V_1}{\partial\theta} - \frac{U_1}{r}\right)\tilde{v}_0 - U_1\frac{\partial\tilde{v}_0}{\partial r} - \frac{V_1}{r}\frac{\partial\tilde{v}_0}{\partial\theta} - \left(\frac{\partial V_1}{\partial r} + \frac{V_1}{r}\right)\tilde{u}_0,\end{aligned} \tag{2.32}$$

$$-\mathrm{i}\omega_0\tilde{w}_1 + \frac{\partial\tilde{w}_1}{\partial\theta} + \mathrm{i}k_0\tilde{p}_1 = -\mathrm{i}k_1\tilde{p}_0 + \mathrm{i}\omega_1\tilde{w}_0 - U_1\frac{\partial\tilde{w}_0}{\partial r} - \frac{V_1}{r}\frac{\partial\tilde{w}_0}{\partial\theta} \tag{2.33}$$

with the continuity equation

$$\frac{\partial\tilde{u}_1}{\partial r} + \frac{\tilde{u}_1}{r} + \frac{1}{r}\frac{\partial\tilde{v}_1}{\partial\theta} + \mathrm{i}k_0\tilde{w}_1 = -\mathrm{i}k_1\tilde{w}_0. \tag{2.34}$$

https://doi.org/10.1017/jfm.2020.1157 Published online by Cambridge University Press

The velocity potential outside satisfies

$$\frac{\partial^2\tilde{\phi}_1}{\partial r^2}+\frac{1}{r}\frac{\partial\tilde{\phi}_1}{\partial r}+\frac{1}{r^2}\frac{\partial^2\tilde{\phi}_1}{\partial\theta^2}-k_0^2\tilde{\phi}_1=2k_0k_1\tilde{\phi}_0. \tag{2.35}$$

The linearised kinematic boundary conditions at $r=1$ are

$$-\mathrm{i}\omega_0\tilde{f}_1+\frac{\partial\tilde{f}_1}{\partial\theta}-\tilde{u}_1=\mathrm{i}\omega_1\tilde{f}_0-V_1\frac{\partial\tilde{f}_0}{\partial\theta}-\frac{\mathrm{d}F_1}{\mathrm{d}\theta}\tilde{v}_0+\frac{\partial U_1}{\partial r}\tilde{f}_0+F_1\frac{\partial\tilde{u}_0}{\partial r}, \tag{2.36}$$

$$\begin{aligned}\tilde{u}_1-\frac{\partial\tilde{\phi}_1}{\partial r}&=\left(-\frac{\partial\Phi_1}{\partial\theta}+V_1\right)\frac{\partial\tilde{f}_0}{\partial\theta}+\left(2\frac{\mathrm{d}F_1}{\mathrm{d}\theta}+\frac{\partial^2\Phi_1}{\partial r^2}-\frac{\partial U_1}{\partial r}\right)\tilde{f}_0\\&\quad+\frac{\mathrm{d}F_1}{\mathrm{d}\theta}\left(\tilde{v}_0-\frac{\partial\tilde{\phi}_0}{\partial\theta}\right)+F_1\left(2\frac{\partial\tilde{f}_0}{\partial\theta}+\frac{\partial^2\tilde{\phi}_0}{\partial r^2}-\frac{\partial\tilde{u}_0}{\partial r}\right).\end{aligned} \tag{2.37}$$

The linearised dynamic condition at $r=1$ is

$$\begin{aligned}&\frac{\rho_2}{\rho_1}\tilde{p}_1-\mathrm{i}\omega_0\tilde{\phi}_1+\frac{\partial\tilde{\phi}_1}{\partial\theta}\\&\quad=\mathrm{i}\omega_1\tilde{\phi}_0-\frac{\partial\Phi_1}{\partial r}\frac{\partial\tilde{\phi}_0}{\partial r}-\frac{\partial\Phi_1}{\partial\theta}\frac{\partial\tilde{\phi}_0}{\partial\theta}+\left(1-\frac{\rho_2}{\rho_1}\right)\tilde{f}_1+\left(2\frac{\partial\Phi_1}{\partial\theta}-\frac{\partial^2\Phi_1}{\partial r\partial\theta}\right)\tilde{f}_0\\&\qquad-F_1\left[\frac{\rho_2}{\rho_1}\frac{\partial\tilde{p}_0}{\partial r}-\mathrm{i}\omega_0\frac{\partial\tilde{\phi}_0}{\partial r}+\frac{\partial^2\tilde{\phi}_0}{\partial r\partial\theta}-2\frac{\partial\tilde{\phi}_0}{\partial\theta}\right]-F_1\left[\frac{\rho_2}{\rho_1}\frac{\partial^2P_0}{\partial r^2}+3\left(\frac{\partial\Phi_0}{\partial\theta}\right)^2\right]\tilde{f}_0\\&\qquad-S\left(\frac{\partial^2\tilde{f}_1}{\partial\theta^2}-k_0^2\,\tilde{f}_1-2k_0k_1\tilde{f}_0-2F_1\frac{\partial^2\tilde{f}_0}{\partial\theta^2}\right).\end{aligned} \tag{2.38}$$

Solutions for the disturbance waves at $O(\delta)$ and $O(\delta\gamma)$ are given in the next section. The dispersion relation is obtained by matching the boundary conditions.

3. Solutions

Solutions for both $O(\delta)$ and $O(\delta\gamma)$ disturbance waves are written as

$$\tilde{\boldsymbol{u}}(r,\theta)=\boldsymbol{u}^{(m)}(r)\,\mathrm{e}^{\mathrm{i}m\theta},\quad \tilde{p}(r,\theta)=p^{(m)}(r)\,\mathrm{e}^{\mathrm{i}m\theta},\quad \tilde{\phi}(r,\theta)=\phi^{(m)}(r)\,\mathrm{e}^{\mathrm{i}m\theta}, \tag{3.1a–c}$$

where m is the azimuthal wavenumber. The resonance condition is when two Kelvin waves of azimuthal wavenumber differing by two are coupled by the quadrupole at $O(\delta)$. The solutions at $O(\delta)$ and $O(\delta\gamma)$ are written as m and $m+2$ waves.

3.1. *Kelvin waves at $O(\delta)$*

The solution at $O(\delta)$ is a Kelvin wave, which is described in appendix B. The Kelvin waves are coupled with the quadrupole field (2.14a–c) through the right-hand sides of (2.31)–(2.33). When two Kelvin waves with azimuthal wavenumber m and $m+2$ appear in the forcing terms on the right-hand side of (2.31)–(2.33), the solution at the $O(\delta\gamma)$ will possess modes for $m-2$, m, $m+2$ and $m+4$. The resonances are between pairs of two adjacent modes separated by two. We focus on the resonance between a pair of Kelvin waves $(m, m+2)$ in this paper, because the cases for $(m-2, m)$, $(m+2, m+4)$ can be obtained by using different value of m.

https://doi.org/10.1017/jfm.2020.1157 Published online by Cambridge University Press

The solution (B1) and (B4) contains coefficients (Kelvin wave amplitudes) α_0 and β_0 that are determined using the boundary conditions. The boundary conditions for wavenumber m become

$$-\mathrm{i}(\omega_0 - m) f_0^{(m)} = u_0^{(m)} = \frac{\mathrm{d}\phi_0{}^{(m)}}{\mathrm{d}r}, \tag{3.2}$$

$$\frac{\rho_2}{\rho_1} p_0^{(m)} - \mathrm{i}(\omega_0 - m)\phi_0^{(m)} = \left(1 - \frac{\rho_2}{\rho_1}\right) f_0^{(m)} + S(m^2 + k_0^2) f_0^{(m)}. \tag{3.3}$$

Substituting $p_0^{(m)}$, $u_0^{(m)}$, $\phi_0^{(m)}$ and $f_0^{(m)}$ (see appendix B) into the equations above, we obtain a set of homogeneous linear equations for $\alpha_0^{(m)}$ and $\beta_0^{(m)}$. For non-trivial $\alpha_0^{(m)}$ and $\beta_0^{(m)}$, the determinant must be zero, which gives the dispersion relation for mode m (see Part 1):

$$\begin{aligned}
&\left[1 + \frac{E_1}{(\omega_0 - m)^2}\left(m - k_0 \frac{\mathrm{K}_{m+1}(k_0)}{\mathrm{K}_m(k_0)}\right)\right] \mathrm{J}_{m+1}(\eta_1) \\
&\quad = \left\{-m\frac{\omega_0 - m}{\omega_0 - m + 2} + \left[\frac{\rho_2}{\rho_1} - E_1 \frac{m}{(\omega_0 - m)(\omega_0 - m + 2)}\right]\left(m - k_0 \frac{\mathrm{K}_{m+1}(k_0)}{\mathrm{K}_m(k_0)}\right)\right\} \\
&\qquad \times \frac{\eta_1}{k_0^2} \mathrm{J}_m(\eta_1),
\end{aligned} \tag{3.4}$$

where $E_1 = 1 - \rho_2/\rho_1 + S(k_0^2 + m^2)$. Here J_m is the Bessel function of the first kind and K_m is the modified Bessel function of the second kind; η_1 is the radial wavenumber defined in (B2). For the second set of Kelvin waves, the azimuthal wavenumber is $m + 2$ in the MSTW instability instead of $m + 1$ in the curvature calculation. The boundary conditions are the same formulae as in (3.3) except that m is replaced by $m + 2$, and similarly for the solution in appendix B. Using the boundary conditions and the solution for the $m +$ 2-mode, we obtain the dispersion relation

$$\begin{aligned}
&\left[1 - \frac{E_2}{(\omega_0 - m - 2)^2}\left(m + 2 + k_0 \frac{\mathrm{K}_{m+1}(k_0)}{\mathrm{K}_{m+2}(k_0)}\right)\right] \mathrm{J}_{m+1}(\eta_2) \\
&\quad = \left\{-(m+2)\frac{\omega_0 - m - 2}{\omega_0 - m - 4} + \left[\frac{\rho_2}{\rho_1} + E_2 \frac{m+2}{(\omega_0 - m - 2)(\omega_0 - m - 4)}\right]\right. \\
&\qquad \left. \times \left(m + 2 + k_0 \frac{\mathrm{K}_{m+1}(k_0)}{\mathrm{K}_{m+2}(k_0)}\right)\right\} \frac{\eta_2}{k_0^2} \mathrm{J}_{m+2}(\eta_2),
\end{aligned} \tag{3.5}$$

where $E_2 = 1 - \rho_2/\rho_1 + S[k_0^2 + (m+2)^2]$ and η_2 is the radial wavenumber for $m + 2$.

The intersection points between the two sets of Kelvin waves give possible candidates for parametric instability. The actual modes can be found by finding the roots for (3.4) and (3.5) with $\omega_0 \in [m, m + 2]$. For Kelvin waves with azimuthal wavenumber m, there are cograde branches going upward where $\omega_0 > m$ and retrograde branches going downward where $\omega_0 < m$ (see figure 2 for $m = 2$). The cograde branches are labelled from the top as the first, second, ... cograde modes, whereas the retrograde branches are labelled from the bottom. The cograde branches of the m waves and the retrograde branches of the $m + 2$ waves cross in $\omega_0 \in [m, m + 2]$ setting up possible modes for resonance. We follow the definition used by Fukumoto (2003) for the case $(\rho_2/\rho_1, S) = (1, 0)$. The principal modes are the intersection point of the first cograde branch for m and the isolated branch for $m + 2$, and also the intersection points of the $i + 1$th cograde branches for m and the ith retrograde branches for $m + 2$. This definition is slightly different from that in § 3 of

https://doi.org/10.1017/jfm.2020.1157 Published online by Cambridge University Press

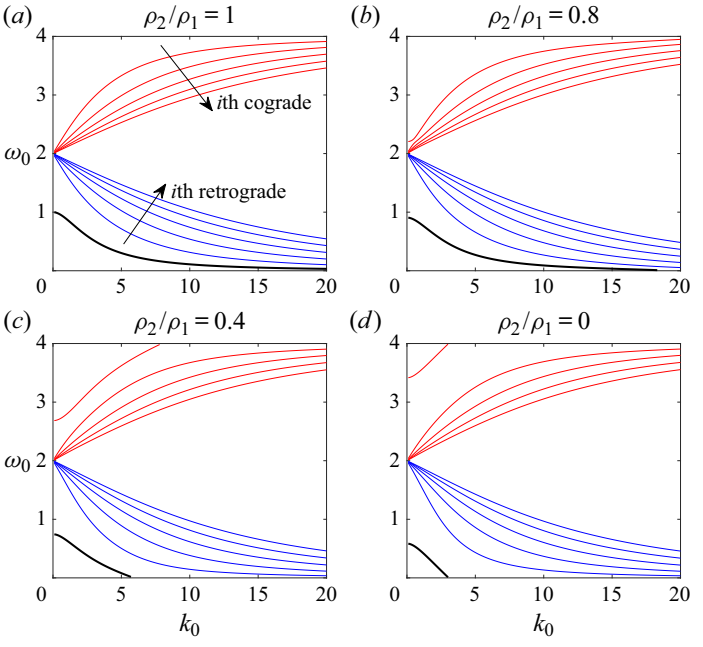


Figure 2. Dispersion curves for the Kelvin wave with $m = 2$ for density ratios from one to zero. Red curves are cograde branches and blue curves are retrograde branches. Only the first five branches of each are plotted. An isolated branch (thick black curve) can be seen below the retrograde branches. Surface tension is zero for all plots.

Part 1 for the curvature instability, where the cograde branches for m never cross the isolated branch for $m + 1$ when $(\rho_2/\rho_1, S) = (1, 0)$.

As discussed in Part 1, density and surface tension act to 'isolate' the first cograde mode when $(\rho_2/\rho_1, S) \neq (1, 0)$. In figure 2, the first cograde mode (the uppermost red curve with the largest value of $|\omega_0 - 2|$) departs from the other cograde modes and shifts upward as the density ratio decreases. The isolated branch (thick black line) also shifts downward from its initial position when $\rho_2/\rho_1 = 1$, and the short-wavelength part (large k_0) of the isolated branch drops below $\omega_0 = m - 2$. On the other hand, when the density ratio increases above one, the situation reverses: the first cograde mode and the isolated mode move closer toward other cograde and retrograde modes. In all cases, Kelvin waves stay neutrally stable. The branch that extends beyond $\omega_0 \in [m - 2, m + 2]$ still has purely real ω_0. A special scenario is two counter-winding helical waves with azimuthal wavenumber $m = -1$ and 1 whose dispersion curves are symmetric about the k_0-axis (figure 3). In this case, the principal modes are always on the k_0-axis, and $\omega_0 = 0$.

3.2. *Resonance at $O(\delta\gamma)$*

The solution of the $O(\delta\gamma)$ disturbances governed by (2.31)–(2.34) is given in appendix A of Fukumoto (2003). We do not reproduce it here, given its complexity. The solution contains undetermined coefficients α_1, β_1 (appearing in the linear systems in (C7) and (C8)) which must be non-zero. The boundary conditions in (2.37) and (2.38) are used to obtain the dispersion relation. Note that in order to include surface tension, we need to compute $\tilde{f}_1$ from (2.36) before using the dynamic condition for the dispersion relation.

https://doi.org/10.1017/jfm.2020.1157 Published online by Cambridge University Press

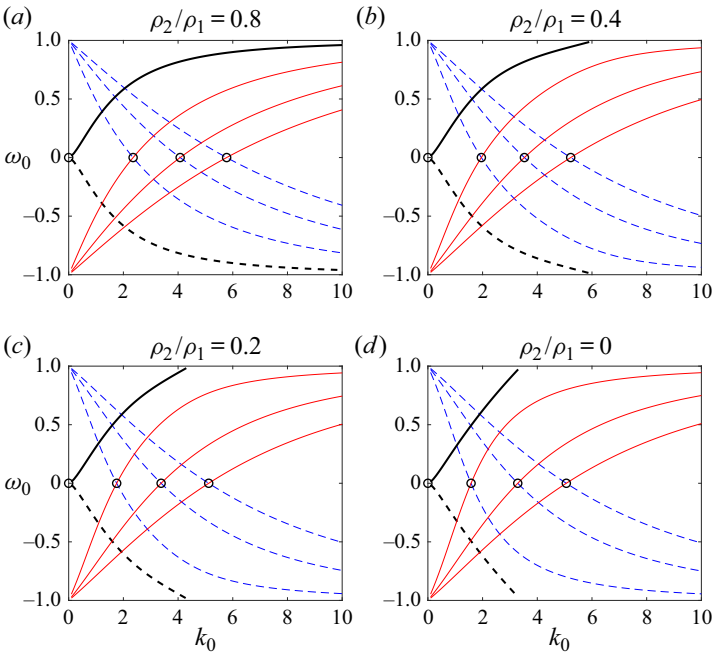


Figure 3. The first three cograde modes of the Kelvin wave for $m = -1$ (red) and the first three retrograde modes of the Kelvin wave for $m = 1$ (blue dashed); their isolated branches (thick solid and dashed) can be seen emanating from $(k_0, \omega_0) = (0, 0)$. Circles are the first four principal modes with $\omega_0 = 0$. Here $S = 0$ for all cases.

In Moore & Saffman (1975), Tsai & Widnall (1976) and Fukumoto (2003), computing $\tilde{f}_1$ is not necessary because $\rho_2/\rho_1 = 1$ and surface tension is omitted.

Substituting the basic solution (2.14*a–c*)–(2.16) into the boundary conditions (2.37) and (2.38) gives

$$\tilde{u}_1 - \frac{\partial \tilde{\phi}_1}{\partial r} = \sin 2\theta \left[\frac{\partial \tilde{\phi}_0}{\partial \theta} - \tilde{v}_0 + \left(1 - \frac{\rho_2}{\rho_1} + 3S\right)\tilde{f}_0 \right] + \frac{1}{2}\cos 2\theta \left[-\left(1 - \frac{\rho_2}{\rho_1} + 3S\right)\frac{\partial \tilde{f}_0}{\partial \theta} + \frac{\partial^2 \tilde{\phi}_0}{\partial r^2} - \frac{\partial \tilde{u}_0}{\partial r} \right]; \tag{3.6}$$

$$\frac{\rho_2}{\rho_1}\tilde{p}_1 - \mathrm{i}\omega_0 \tilde{\phi}_1 + \frac{\partial \tilde{\phi}_1}{\partial \theta} = \mathrm{i}\omega_1 \tilde{\phi}_0 + \sin 2\theta \frac{\partial \tilde{\phi}_0}{\partial r} + \left(1 - \frac{\rho_2}{\rho_1}\right)\tilde{f}_1 - \frac{1}{2}\left(-1 - \frac{\rho_2}{\rho_1} + 3S\right)\cos 2\theta \frac{\partial \tilde{\phi}_0}{\partial \theta} + \frac{3}{2}\left(1 - \frac{\rho_2}{\rho_1} + 2S\right)\cos 2\theta \tilde{f}_0 - \frac{1}{2}\cos 2\theta \left[\frac{\rho_2}{\rho_1}\frac{\partial \tilde{p}_0}{\partial r} - \mathrm{i}\omega_0 \frac{\partial \tilde{\phi}_0}{\partial r} + \frac{\partial^2 \tilde{\phi}_0}{\partial r \partial \theta} \right] - S\left(\frac{\partial^2 \tilde{f}_1}{\partial \theta^2} - k_0^2 \tilde{f}_1 - 2k_0 k_1 \tilde{f}_0 - \cos 2\theta \frac{\partial^2 \tilde{f}_0}{\partial \theta^2} \right). \tag{3.7}$$

https://doi.org/10.1017/jfm.2020.1157 Published online by Cambridge University Press

	k_0	σ_{1max}	Δk_1
Fukumoto (2003)	2.504982369	0.5707533917	2.145502816
	4.349076726	0.5694562098	3.518286549
	6.174012330	0.5681222780	4.883945142
	7.993536550	0.5671646287	6.247280752
	9.810807288	0.5664714116	7.609553122
Present work	2.50498236892631	0.570753391682824	2.14548262220342
	4.34907672483174	0.569456209750883	3.51827586739091
	6.17401232939918	0.568122278011138	4.88395077269524
	7.99353654972030	0.567164628732371	6.24727962008910
	9.81080728697861	0.566471411560612	7.60954536410281

Table 1. For the $m = -1$ and 1 resonances, present results for $\rho_2/\rho_1 = 1$ compared with table 1 of Fukumoto (2003). Each row represents a principal mode with $k_0 = 0$.

Using the above equations, we obtain two sets of equations for m and $m + 2$ in (C1)–(C4). They can be written as two inhomogeneous linear systems (C7) and (C8) for α_1 and β_1. The dispersion relation (C14) is given by requiring that α_1 and β_1 do not vanish (see the details in appendix C). A dispersion relation for (k_1, ω_1) determines the stability, and the flow is unstable for $\mathrm{Im}\{\omega_1\} > 0$. The maximum growth rate σ_{1max} is given by the maximum imaginary part of ω_1 at $k_1 = 0$; and the half-bandwidth of instability, Δk_1, by the range over which the imaginary part of ω_1 does not vanish. The expressions for all formulae are too cumbersome to handle manually, and so computer symbolic algebra is utilised to obtain the dispersion relation (C14) and ω_1 and Δk_1. A description of procedure is given in detailed in appendix C, and the symbolic algebra files are provided in the supplementary material available at https://doi.org/10.1017/jfm.2020.1157 (as Matlab scripts). We show numerical results for $m = -1$ and 1 in the next section, followed by the case for $m \geqslant 0$ in § 5.

4. Resonance between waves $m = -1$ and 1

We first discuss the special case of the resonance pair $(-1, 1)$ in this section. When $m = -1$, the resonance is between right- and left-handed helical waves. Fukumoto (2003) gives a detailed discussion of this resonance pair. Widnall *et al.* (1974) and Moore & Saffman (1975) imply that the stationary mode is most unstable. The two dispersion curves are mirrored about $\omega_0 = 0$ (see figure 3), and therefore their principal modes are exactly on the k_0-axis.

4.1. *Principal modes ($\omega_0 = 0$)*

We substitute $m = -1$ and $\omega_0 = 0$ for the principal modes of stationary waves (circles in figure 3). The maximum growth rate σ_{1max} and half the instability bandwidth Δk_1 are then calculated using computer symbolic algebra. To verify the result of the symbolic calculation, results for $(\rho_2/\rho_1, S) = (1, 0)$ are compared with those in Fukumoto (2003) in table 1. The present study has σ_{1max} accurate to 10 significant figures and Δk_1 up to five significant figures. As seen in figure 3, the first principal mode at $(k_0, \omega_0) = (0, 0)$ is independent of ρ_2/ρ_1 and S, so we do not include it in the comparison here.

The principal modes' maximum growth rates and instability half-bandwidths are plotted as functions of ρ_2/ρ_1 in figure 4(*a*) for $S = 0$. The second principal mode (blue curve) is

https://doi.org/10.1017/jfm.2020.1157 Published online by Cambridge University Press

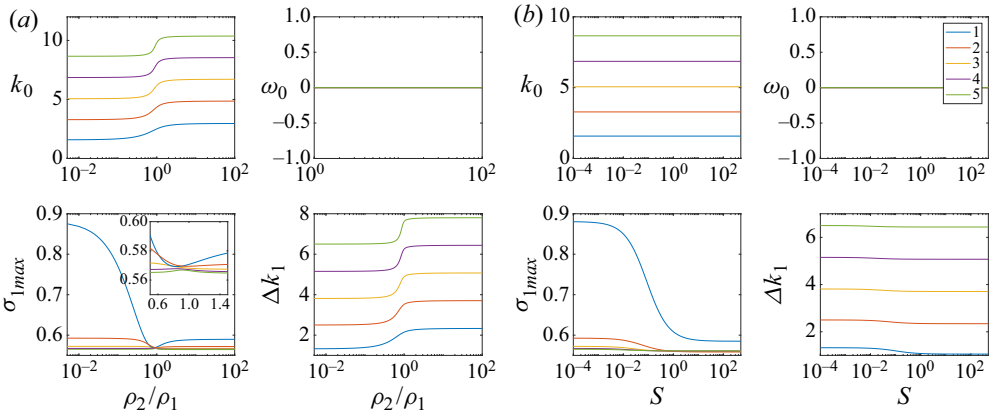


Figure 4. Principal modes $(k_0, 0)$ for $(m, m+2) = (-1, 1)$, the maximum growth rate σ_{1max} and the instability half-bandwidth Δk_1 plotted versus: (*a*) density ratio $\rho_2/\rho_1 \in [0.005, 100]$ for $S = 0$; (*b*) surface tension $S \in [0, 500]$ with $\rho_2/\rho_1 = 0.001$. The second to sixth principal modes are the blue, red, amber, purple and green curves.

the most unstable mode. The largest growth rate is at $\rho_2/\rho_1 = 0$ with a value of $\sigma_{1max} = 0.882$. The least unstable density ratio is 0.915, where the second and third principal modes have a growth rate of 0.5696. The instability half-bandwidth, Δk_1, is strongly correlated with the axial wavenumber k_0, and the principal mode with higher k_0 has wider instability bandwidth. Figure 4(*b*) shows the effect of surface tension when $\rho_2/\rho_1 = 0.001$. The density ratio 0.001 is picked because it is close to the typical ratio between air and water. Surface tension merely changes the locations of principal modes. The second principal mode dominates the instability. The growth rate is 0.8803 at $S = 10^{-4}$ and drops to 0.585 when $S = 500$.

The growth rate and the instability half-bandwidth are calculated for large k_0 in figure 5 with different values of $\rho_2/\rho_1 \in [0, 1]$ and $S \in [0, 100]$. Density only has an effect on the growth rate σ_{1max} for principal modes with $k_0 < 10$. The growth rates for different values of ρ_2/ρ_1 and S all converge to a fixed value 0.5625 as $k_0 \to \infty$. The short-wavelength limit given in (5.13), (5.14) of Fukumoto (2003) for $(\rho_2/\rho_1, S) = (1, 0)$ as

$$\sigma_{1max} \approx \frac{9}{16}\left(1 + \frac{1}{12k_0} - \frac{7}{48k_0^2} + \frac{5}{64k_0^3}\right), \tag{4.1a}$$

$$\Delta k_1 \approx \frac{3k_0}{4}\left(1 + \frac{1}{3k_0} + \frac{5}{24k_0^3}\right), \tag{4.1b}$$

is plotted as dashed lines in figure 5.

4.2. *Non-principal modes*

For stationary waves $m = \pm 1$, non-principal modes are intersection points where $\omega_0 \neq 0$. Theoretically, an infinite number of non-principal modes exist because the two Kelvin waves have an infinite number of intersection points. Here we show only those non-principal modes for $k_0 \in [0, 20]$ and $\omega_0 \in (0, 0.5]$ in figure 6. In the case $\rho_2/\rho_1 = 1$ and $S = 0$, the growth rates of non-principal modes are at least two orders of magnitude smaller than that of the principal modes (see figure 6*a*). As the density ratio decreases to

https://doi.org/10.1017/jfm.2020.1157 Published online by Cambridge University Press

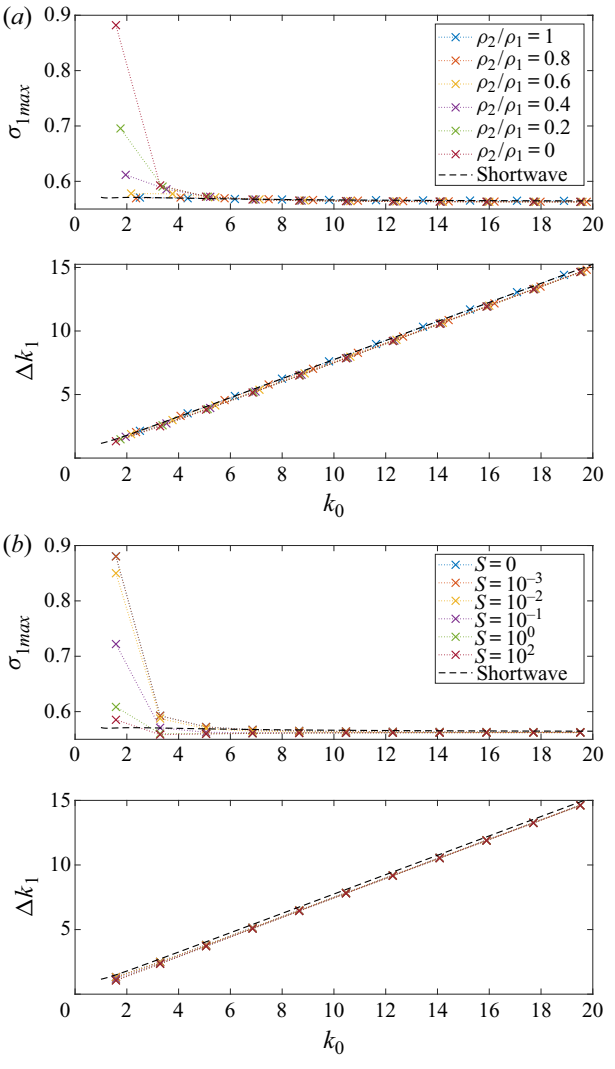


Figure 5. Maximum growth rate σ_{1max} and unstable half-bandwidth Δk_1 of principal modes with axial wavenumber $k_0 < 20$ for helical waves $(m, m+2) = (-1, 1)$: (*a*) different ρ_2/ρ_1 with $S = 0$; (*b*) different S with $\rho_2/\rho_1 = 0.001$. The dashed line is the short-wavelength asymptotic result (4.1) for $\rho_2/\rho_1 = 1$ and $S = 0$.

zero, the maximum growth rates of non-principal modes grow and become one order of magnitude smaller than those of the principal modes. The trend reverses for increasing surface tension. The maximum growth rate of non-principal modes is one order of magnitude less than that of the principal modes and that difference widens to more than two orders of magnitude for $S = 10$ in figure 6(*b*). With variations in either density or surface tension, the instability of the principal modes always dominates over non-principal modes.

5. Resonance between waves m and $m + 2$ ($m \geqslant 0$)

We continue to explore resonant pairs of $(m, m + 2)$ other than $(-1, 1)$. Among those pairs, the case of $(0, 2)$ is particular interesting. As Fukumoto (2003) states, this is a result

https://doi.org/10.1017/jfm.2020.1157 Published online by Cambridge University Press

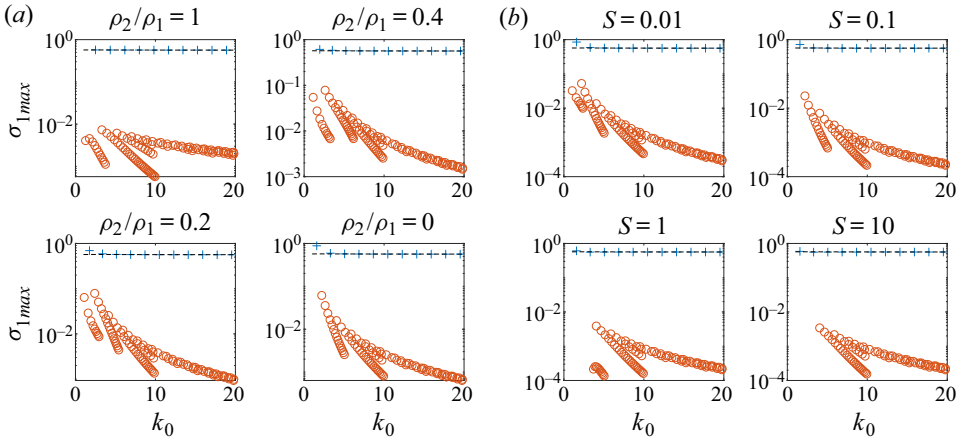


Figure 6. Maximum growth rate σ_{1max} for the modes of the $(-1, 1)$ resonance with variations of (*a*) ρ_2/ρ_1 for $S = 0$ and (*b*) S for $\rho_2/\rho_1 = 0.001$. Principal modes (with $k_0 \leqslant 20$) are marked by blue crosses whereas other modes are red circles. The black dashed line is the short-wavelength asymptotic result (4.1) for $\rho_2/\rho_1 = 1$ and $S = 0$.

of its resistance to viscous dissipation when the Reynolds number is not sufficiently large (Éloy & Le Dizès 2001). We first discuss the (0, 2) resonant pair, followed by other helical waves.

5.1. *The case $m = 0$*

We calculate the growth rate σ_{1max} and half the unstable bandwidth Δk_1 for the first five principal modes. The definition of principal modes is the same as in Éloy & Le Dizès (2001) and Fukumoto (2003): the first principal mode is the intersection between the first cograde mode for $m = 0$ and the isolated mode for $m = 2$, the second principal mode is the second cograde mode for $m = 0$ intersected by the first retrograde mode for $m = 2$, and so on. The location (k_0, ω_0) of the principal modes in figure 7(*a*) shows that k_0 shifts to lower wavelengths as the density ratio ρ_2/ρ_1 drops below one. The growth rate of the first principal mode has a cusp at $\rho_2/\rho_1 = 0.215$ with $\sigma_{1max} \approx 4.32$. The mode is then stable below $\rho_2/\rho_1 < 0.215$, and this mode does not exist for $\rho_2/\rho_1 \lesssim 0.09$ because the two branches on which the first principal mode is located do not cross each other when the density ratio drops below 0.09 (as explained in § 3.1). The third principal mode is the most unstable with $\sigma_{1max} = 0.5668647793$ for $\rho_2/\rho_1 = 1$ in the calculation of Fukumoto (2003). In our calculation with density variations, the second principal mode is the most unstable mode as $\rho_2/\rho_1 \to 0$ with $\sigma_{1max} = 0.6028$, whereas the first principal mode is the most unstable for $\rho_2/\rho_1 \to 100$ with $\sigma_{1max} = 0.6167$. The trend in Δk_1 is very similar to that in k_0: as the density ratio decreases the unstable bandwidth decreases. We also extend our calculation to other principal modes with higher axial wavenumber k_0 in figure 9. The growth rate is asymptotically close to that of (4.1) in the short-wavelength regime for $\rho_2/\rho_1 = 1$. For large k_0, Δk_1 increases linearly with k_0 and the slopes are identical except for $k_0 < 4$.

The disturbed boundary of the first principal mode in the (0, 2) resonance is shown in figure 8. The shape of the resonant disturbance transitions from helical waves to bulging waves as density ratio decreases. The axial wavelength of the disturbance increases (k_0 decreases) as the density ratio decreases. This is due to the effect of density on the Kelvin

https://doi.org/10.1017/jfm.2020.1157 Published online by Cambridge University Press

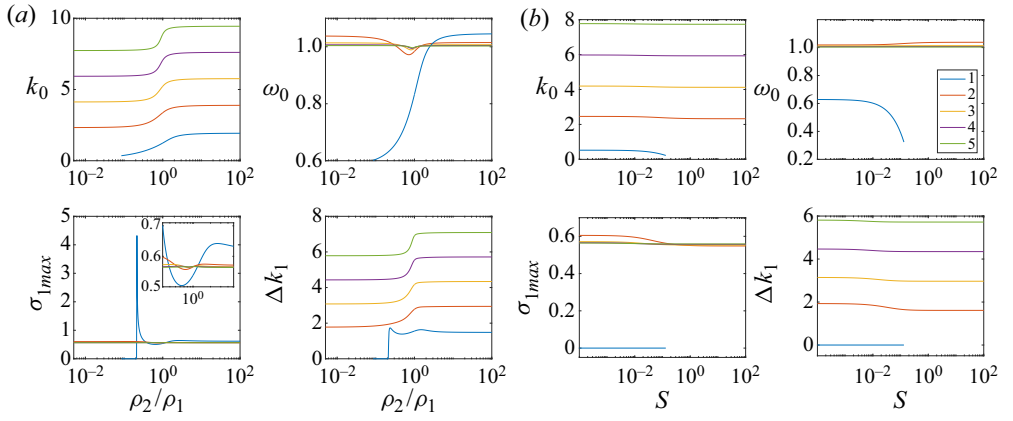


Figure 7. Principal modes for $(m, m+2) = (0, 2)$, maximum growth rate σ_{1max} and the instability half-bandwidth Δk_1 plotted versus: (*a*) density ratio $\rho_2/\rho_1 \in [0.005, 100]$ for $S = 0$; (*b*) surface tension $S \in [0, 500]$ at $\rho_2/\rho_1 = 0.2$. The first to fifth principal modes are the blue, red, amber, purple and green curves.

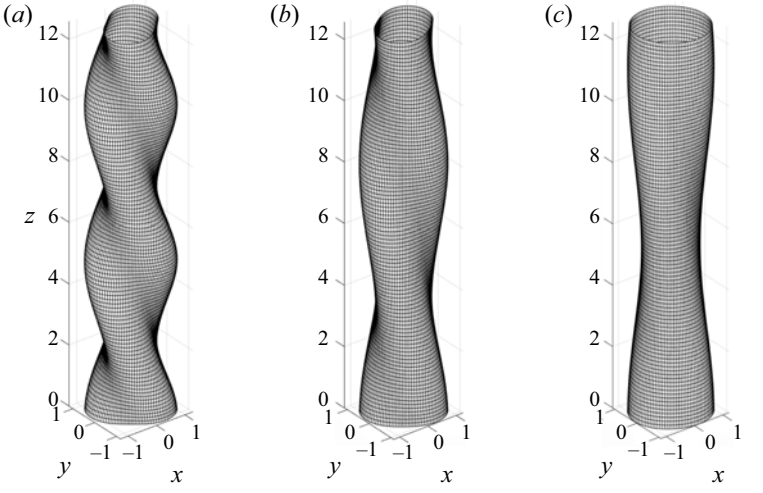


Figure 8. Disturbed boundary for the first principal mode of the $(0, 2)$ resonance with different density ratio: (*a*) $\rho_2/\rho_1 = 1$, $(k_0, \omega_0) = (1.242233570, 0.8326707800)$; (*b*) $\rho_2/\rho_1 = 0.4$, $(k_0, \omega_0) = (0.7529505549, 0.6784320753)$; (*c*) $\rho_2/\rho_1 = 0.22$, $(k_0, \omega_0) = (0.5503572727, 0.6335367950)$. The disturbance transitions from helical mode into bulging mode as ρ_2/ρ_1 decreases.

wave dispersion relation. Consequently the location of the intersection point changes. Given that the strain field is applied uniformly along the z-direction, bulging modes (figure 8*c*) are more susceptible to the strain field. Because a bulging mode is axisymmetric with respect to the z-axis, it has no preferred direction and can deform more easily. For helical modes, the twist makes the core structure vary constantly per unit length in z, so that the core is more resistant to a strain of uniform direction.

The dependence on surface tension S is shown in figure 7(*b*) for $\rho_2/\rho_1 = 0.2$. The first principal mode does not exist as surface tension increases to a value above $S \approx 0.14$ and is always unstable below that threshold. The effect on the other four principal modes is not significant. The second principal mode (red curve) has the biggest drop in σ_{1max} from a value of 0.6049 to 0.5482 at $S = 100$. The mitigation of the instability by surface tension is

https://doi.org/10.1017/jfm.2020.1157 Published online by Cambridge University Press

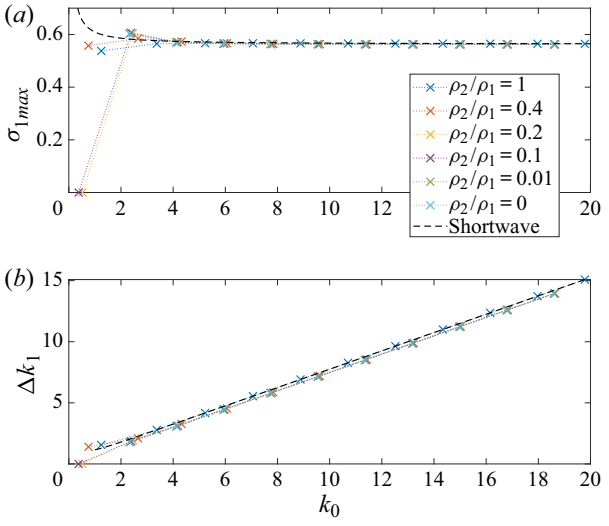


Figure 9. Maximum growth rate σ_{1max} and unstable half-bandwidth Δk_1 of principal modes with axial wavenumber $k_0 < 20$ for $(m, m+2) = (0, 2)$ with different ρ_2/ρ_1 with $S = 0$. The dashed line is the short-wavelength asymptotic result (4.1) for $\rho_2/\rho_1 = 1$.

as expected, since surface tension makes the interface more resistant to deformation when subjected to a strain.

5.2. *Other pairs* $(m, m+2)$

Moving on to higher resonance pairs, e.g. $(m, m+2) = (4, 6)$, we found the change in the positions (k_0, ω_0) of principal modes (see figure 10*a*) to be qualitatively similar to that for the $(0, 2)$ pair. The first principal mode (in blue in figure 10) disappears near a larger density ratio at the value of $\rho_2/\rho_1 = 0.72$. The most significant difference is how the growth rate behaves before the first principal mode disappears. For $(m, m+2) = (0, 2)$, the growth rate of the first principal mode increases drastically and then drops to zero before the first principal mode vanishes (figure 7*a*), whereas for $(m, m+2) = (4, 6)$, σ_{1max} plunges to zero in figure 10(*a*) and never exceeds 0.6. The dependence on surface tension S is shown in figure 10(*b*). The growth rate σ_{1max} decreases only slightly, and is almost independent of surface tension for $S \gtrsim 1$.

Resonance pairs with higher azimuthal wavenumber m have smaller growth rate σ_{1max} for the MSTW instability, whereas the curvature instability is more unstable for larger m (see Chang & Llewellyn Smith 2021). In figure 11 we plot the maximum growth rate among intersection points (resonant modes) that include the principal modes and a few non-principal modes for axial wavenumber $k_0 \leqslant 20$, as a function of density ratio ρ_2/ρ_1. The maximum growth rate decreases as m increases. This is due to the strain field, which kills the small-scale disturbances on the boundary. For a fixed value of m, the growth rate is constant for very large and small ρ_2/ρ_1, and the curve has a dip in the middle at $\rho_2/\rho_1 = 0.925$. That is where the most unstable mode (that with the largest growth rate) jumps from one intersection point of Kelvin waves to another. As shown in figure 12, the most unstable mode, represented by a black dot, switches from the seventh principal mode to the fourth principal mode as the density ratio increases from 0.925 to 1.069.

Given that the whole calculation is based on discrete intersection points of Kelvin waves, the largest growth rate among all modes can have a discontinuity while it switches from

https://doi.org/10.1017/jfm.2020.1157 Published online by Cambridge University Press

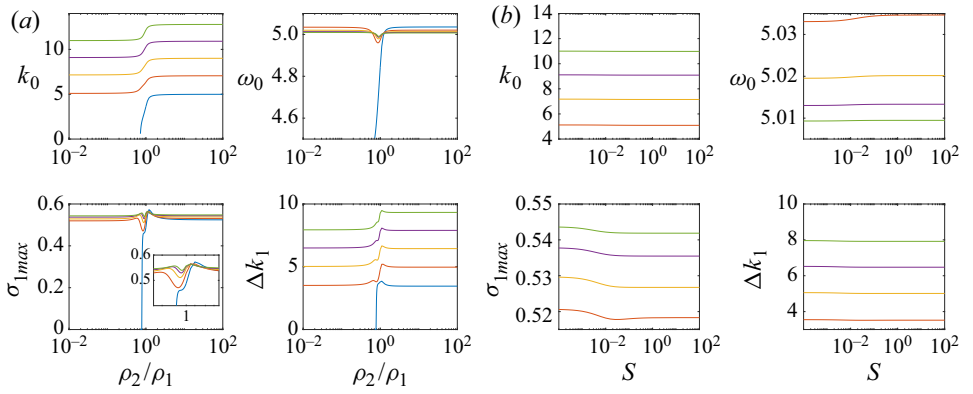


Figure 10. Principal modes for $(m, m+2) = (4, 6)$, the maximum growth rate σ_{1max} and the instability half-bandwidth Δk_1 are plotted versus: (*a*) density ratio $\rho_2/\rho_1 \in [0.01, 100]$ for $S = 0$; (*b*) surface tension $S \in [0, 100]$ at $\rho_2/\rho_1 = 0.2$. The first to fifth principal modes are the blue, red, amber, purple and green curves.

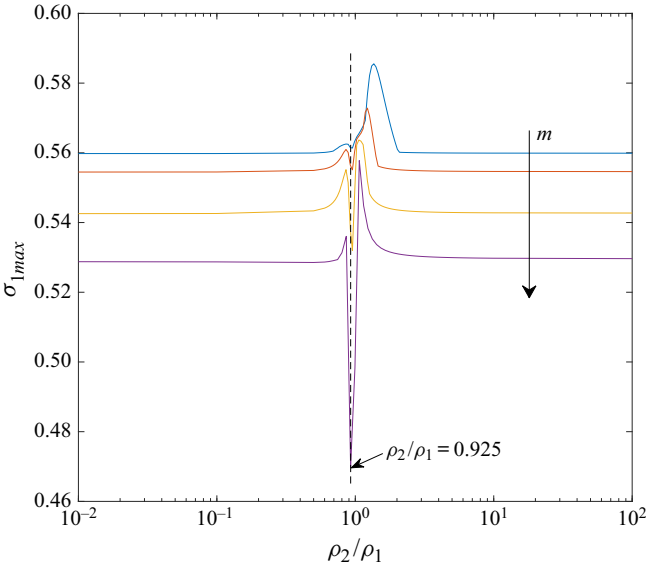


Figure 11. Maximum growth rate for modes with $\rho_2/\rho_1 \in [0.01, 100]$ and $S = 0$. Blue, red, amber and purple curves are for resonance pairs $(m, m+2)$, $m = 2, 4, 8$ and 16, respectively. The vertical dashed line is the value $\rho_2/\rho_1 = 0.925$ where the growth rate has a dip.

one intersection point to another. That happens when the previous most unstable mode had decayed or disappeared, and another mode takes over. The instability of a resonant mode is a function of its location (k_0, ω_0) and the location is a function of density ratio and surface tension. The migrations of the first cograde mode and the isolated mode discussed in § 3 also have a huge influence on the location of intersection points.

6. Conclusion

The parametric instability of a vortex column subjected to a weak strain field has been investigated for varying density ratio and surface tension. The instability, the

https://doi.org/10.1017/jfm.2020.1157 Published online by Cambridge University Press

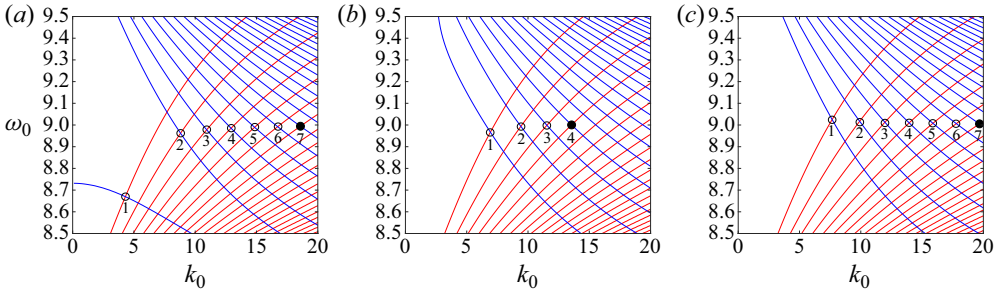


Figure 12. Intersection points of the pair $(m, m+2) = (8, 10)$: (*a*) $\rho_2/\rho_1 = 0.925$; (*b*) $\rho_2/\rho_1 = 1.069$; and (*c*) $\rho_2/\rho_1 = 10$. Surface tension is zero. Principal modes are labelled by numbered circles; the black dot is the mode with largest growth rate. The most unstable mode switches from the seventh principal mode to the fourth principal mode, then back to the seventh, causing the discontinuity in σ_{1max}.

MSTW instability, is the result of the resonance between two Kelvin waves of azimuthal wavenumber m and $m+2$. The resonance is fed by a quadrupole field which comes from the correction to the basic state at $O(\gamma)$. We have extended the calculation by Fukumoto (2003) to a parameter space $(\rho_2/\rho_1, S)$, where $(\rho_2/\rho_1, S) = (1, 0)$ is the previous result.

Two distinguished types of resonances are examined. The first corresponds to stationary helical waves with azimuthal wavenumber $m = \pm 1$. The strained vortex is most unstable when the density ratio is very small ($\rho_2/\rho_1 \to 0$): the maximum growth rate is $\sigma_{1max} \approx 0.88$ compared with a minimum of 0.57 near $\rho_2/\rho_1 = 1$. Surface tension mitigates the instability of the vortex for $S > 0.01$, and the maximum growth rate drops from 0.88 to 0.58 as $S \to \infty$. We have also shown that the most unstable modes are dominated by the principal modes in the resonances for $m = \pm 1$ stationary waves. The second type of resonances is for azimuthal wavenumber $m \geqslant 0$, and $m = 0$ is a particular case of bulging modes. For the $(0, 2)$ resonance, the maximum growth rate from the first principal mode is maximised near $\rho_2/\rho_1 = 0.215$ with a very large value, and that mode vanishes as $\rho_2/\rho_1 \to 0$ whereas the second principal mode takes over to become most unstable. We have also shown that the maximum growth rate decreases as the azimuthal wavenumber m increases, which is in contrast to the curvature instability.

In the recent study by Hattori *et al.* (2019) using DNS, the short-wavelength MSTW instability (the elliptic instability) was shown to be more unstable than the curvature instability for a vortex ring of Gaussian core structure. This result demonstrates the validity of the theoretical prediction in Blanco-Rodriguez & Le Dizès (2016) of the elliptic instability for the Batchelor vortex (a vortex with a Gaussian core). Furthermore, the analytical result of curvature instability for a Gaussian core (Blanco-Rodriguez & Le Dizès 2017) has also been confirmed in Hattori *et al.* (2019). This is the first numerical evidence for the curvature instability after its discovery by Hattori & Fukumoto (2003) and Fukumoto & Hattori (2005) for vortex rings. The present study considers uniform cores with a jump in density across the boundary. It would be of interest to extend this result to continuous vorticity and density distributions. It will be more complicated to carry out a full numerical simulation for this kind of problem with large density jumps at the boundary of the vortices. Direct numerical simulations to detect the curvature and MSTW instabilities of vortices with density differences hence remain tasks for future investigation.

Supplementary material. Supplementary material is available at https://doi.org/10.1017/jfm.2020.1157.

Acknowledgement. Conversations with L. Lacaze were helpful.

https://doi.org/10.1017/jfm.2020.1157 Published online by Cambridge University Press

Funding. This work was supported by the National Science Foundation under award number CBET-1706934.

Declaration of interests. The authors report no conflict of interest.

Author ORCIDs.
Ching Chang https://orcid.org/0000-0003-0923-2644;
Stefan G. Llewellyn Smith https://orcid.org/0000-0002-1419-6505.

Appendix A. The mean-flow solution

The basic solution is written as a perturbation series in γ in (2.11*a–c*). The leading-order solution is the Rankine vortex with a circular boundary. The pressure comes from solving

$$-\frac{V_0^2}{r} = -\frac{\partial P_0}{\partial r} \tag{A1}$$

inside the vortex and the Bernoulli equation outside. The pressure at $r = 1$ is matched using

$$\frac{\rho_2}{\rho_1} P_0 + \frac{1}{2}\left(\frac{\partial \Phi_0}{\partial \theta}\right)^2 = S. \tag{A2}$$

At $O(\gamma)$, (2.12*a*,*b*)–(2.15) give

$$\frac{\partial U_1}{\partial \theta} - 2V_1 = -\frac{\partial P_1}{\partial r}, \tag{A3}$$

$$2U_1 + \frac{\partial V_1}{\partial \theta} = -\frac{1}{r}\frac{\partial P_1}{\partial \theta}, \tag{A4}$$

$$\frac{\partial U_1}{\partial r} + \frac{U_1}{r} + \frac{1}{r}\frac{\partial V_1}{\partial \theta} = 0 \tag{A5}$$

for $r < 1 + \gamma F_1$ and

$$\frac{\partial^2 \Phi_1}{\partial r^2} + \frac{1}{r}\frac{\partial \Phi_1}{\partial r} + \frac{1}{r^2}\frac{\partial^2 \Phi_1}{\partial \theta^2} = 0 \tag{A6}$$

for $r > 1 + \gamma F_1$. The matching condition from (2.9) and (2.10), linearised on $r = 1$, is

$$U_1 - \frac{\mathrm{d}F_1}{\mathrm{d}\theta} = 0, \tag{A7}$$

$$\frac{\partial \Phi_1}{\partial r} - \frac{\mathrm{d}F_1}{\mathrm{d}\theta} = 0, \tag{A8}$$

$$\frac{\rho_2}{\rho_1} P_1 + \frac{\partial \Phi_1}{\partial \theta} + F_1\left(\frac{\rho_2}{\rho_1} - 1\right) = -S\left(F_1 + \frac{\partial^2 F_1}{\partial \theta^2}\right). \tag{A9}$$

https://doi.org/10.1017/jfm.2020.1157 Published online by Cambridge University Press

Appendix B. The solution for Kelvin waves

Kelvin waves satisfying (2.23)–(2.27) with azimuthal wavenumber m are given by

$$\left.\begin{aligned} p_0^{(m)} &= \mathrm{J}_m(\eta_1 r)\beta_0^{(m)}, \\ u_0^{(m)} &= \frac{\mathrm{i}}{\omega_0 - m + 2}\left[-\frac{m}{r}\mathrm{J}_m(\eta_1 r) + \frac{\omega_0 - m}{\omega_0 - m - 2}\eta_1 \mathrm{J}_{m+1}(\eta_1 r)\right]\beta_0^{(m)}, \\ v_0^{(m)} &= \frac{1}{\omega_0 - m + 2}\left[\frac{m}{r}\mathrm{J}_m(\eta_1 r) + \frac{2}{\omega_0 - m - 2}\eta_1 \mathrm{J}_{m+1}(\eta_1 r)\right]\beta_0^{(m)}, \\ w_0^{(m)} &= \frac{k_0}{\omega_0 - m}\mathrm{J}_m(\eta_1 r)\beta_0^{(m)} \end{aligned}\right\} \tag{B1}$$

for $r < 1 + \tilde{f}_0$. The radial wavenumber is

$$\eta_1^2 = \left[\frac{4}{(\omega_0 - m)^2} - 1\right]k_0^2. \tag{B2}$$

The boundary disturbance is given by

$$f_0^{(m)} = \frac{-1}{\mathrm{i}(\omega_0 - m)}u_0^{(m)}, \tag{B3}$$

using the kinematic boundary condition. For $r > 1 + \tilde{f}_0$,

$$\phi_0^{(m)} = \mathrm{K}_m(k_0 r)\alpha_0^{(m)}. \tag{B4}$$

The $(m + 2)$ waves are obtained by replacing m in the formulae by $m + 2$. Appropriate recurrence relations are then used to reduce the order of the Bessel functions.

Appendix C. Solvability conditions and dispersion relation for (k_1, ω_1)

Writing the boundary conditions (2.37) and (2.38) for the $O(\delta\gamma)$ solutions gives

$$\begin{aligned} u_1^{(m)} - \frac{\mathrm{d}\phi_1}{\mathrm{d}r}^{(m)} &= -\frac{m+2}{2}\phi_0^{(m+2)} - \frac{\mathrm{i}}{2}v_0^{(m+2)} + \frac{1}{4}\left[\frac{\mathrm{d}^2\phi_0}{\mathrm{d}r^2}^{(m+2)} - \frac{\mathrm{d}u_0}{\mathrm{d}r}^{(m+2)}\right] \\ &\quad + \frac{\mathrm{i}}{2}\left(1 - \frac{\rho_2}{\rho_1} + 3S\right)f_0^{(m+2)} - \frac{\mathrm{i}(m+2)}{4}\left(1 - \frac{\rho_2}{\rho_1} + 3S\right)f_0^{(m+2)}, \end{aligned} \tag{C1}$$

$$\begin{aligned} &\frac{\rho_2}{\rho_1}p_1^{(m)} - \mathrm{i}(\omega_0 - m)\phi_1^{(m)} \\ &\quad = \mathrm{i}\omega_1\phi_0^{(m)} - \frac{1}{4}\left[\frac{\rho_2}{\rho_1}\frac{\mathrm{d}p_0}{\mathrm{d}r}^{(m+2)} - \mathrm{i}(\omega_0 - m)\frac{\mathrm{d}\phi_0}{\mathrm{d}r}^{(m+2)}\right] \\ &\qquad - \frac{\mathrm{i}(m+2)}{4}\left(-1 - \frac{\rho_2}{\rho_1} + 3S\right)\phi_0^{(m+2)} + \frac{3}{4}\left(1 - \frac{\rho_2}{\rho_1} + 2S\right)f_0^{(m+2)} \\ &\qquad + S\left[2k_0k_1f_0^{(m)} - \frac{(m+2)^2}{2}f_0^{(m+2)}\right] \\ &\qquad + \left[1 - \frac{\rho_2}{\rho_1} + S(m^2 + k_0^2)\right]f_1^{(m)} \end{aligned} \tag{C2}$$

https://doi.org/10.1017/jfm.2020.1157 Published online by Cambridge University Press

for wave m, and

$$u_1^{(m+2)} - \frac{\mathrm{d}\phi_1}{\mathrm{d}r}^{(m+2)} = \frac{m}{2}\phi_0^{(m)} + \frac{\mathrm{i}}{2}v_0^{(m)} + \frac{1}{4}\left[\frac{\mathrm{d}^2\phi_0}{\mathrm{d}r^2}^{(m)} - \frac{\mathrm{d}u_0}{\mathrm{d}r}^{(m)}\right] - \frac{\mathrm{i}}{2}\left(1 - \frac{\rho_2}{\rho_1} + 3S\right)f_0^{(m)} - \frac{\mathrm{i}m}{4}\left(1 - \frac{\rho_2}{\rho_1} + 3S\right)f_0^{(m)}, \tag{C3}$$

$$\begin{aligned}\frac{\rho_2}{\rho_1}p_1^{(m+2)} - \mathrm{i}(\omega_0 - m - 2)\phi_1^{(m+2)} &= \mathrm{i}\omega_1\phi_0^{(m+2)} - \frac{1}{4}\left[\frac{\rho_2}{\rho_1}\frac{\mathrm{d}p_0}{\mathrm{d}r}^{(m)} - \mathrm{i}(\omega_0 - m - 2)\frac{\mathrm{d}\phi_0}{\mathrm{d}r}^{(m)}\right] \\ &\quad - \frac{\mathrm{i}m}{4}\left(-1 - \frac{\rho_2}{\rho_1} + 3S\right)\phi_0^{(m)} + \frac{3}{4}\left(1 - \frac{\rho_2}{\rho_1} + 2S\right)f_0^{(m)} \\ &\quad + S\left[2k_0k_1f_0^{(m+2)} - \frac{m^2}{2}f_0^{(m)}\right] \\ &\quad + \left\{1 - \frac{\rho_2}{\rho_1} + S[(m+2)^2 + k_0^2]\right\}f_1^{(m+2)}\end{aligned} \tag{C4}$$

for wave $m+2$ (cf. (4.8) and (4.9) in Fukumoto (2003), for $\rho_2/\rho_1 = 1$, $S = 0$). Unlike the case of Tsai & Widnall (1976) and Fukumoto (2003), f_1 needs to be obtained from the above equations in order to calculate the dispersion relation. We have

$$f_1^{(m)} = \frac{-1}{\mathrm{i}(\omega_0 - m)}\left[u_1^{(m)} + \mathrm{i}\omega_1 f_0^{(m)} + \frac{\mathrm{i}}{2}v_0^{(m+2)} + \frac{\mathrm{i}(m+1)}{2}f_0^{(m+2)} + \frac{1}{4}\frac{\mathrm{d}u_0}{\mathrm{d}r}^{(m+2)}\right], \tag{C5}$$

$$f_1^{(m+2)} = \frac{-1}{\mathrm{i}(\omega_0 - m - 2)}\left[u_1^{(m+2)} + \mathrm{i}\omega_1 f_0^{(m+2)} - \frac{\mathrm{i}}{2}v_0^{(m)} + \frac{\mathrm{i}(m+1)}{2}f_0^{(m)} + \frac{1}{4}\frac{\mathrm{d}u_0}{\mathrm{d}r}^{(m)}\right]. \tag{C6}$$

The dispersion relation relating k_1 and ω_1 for disturbances at $O(\delta\gamma)$ is determined as follows. The $O(\delta\gamma)$ disturbance satisfies (2.31)–(2.35) with undetermined coefficients (wave amplitudes) α_1, β_1 in the solution, which need to be determined using the boundary conditions at $O(\delta\gamma)$. The boundary conditions (C1) and (C2) for mode m lead to an inhomogeneous linear system of the form

$$\begin{bmatrix} M_{11} & M_{12} \\ M_{21} & M_{22} \end{bmatrix}\begin{bmatrix} \alpha_1^{(m)} \\ \beta_1^{(m)} \end{bmatrix} = \begin{bmatrix} F_1 \\ F_2 \end{bmatrix}, \tag{C7}$$

whereas (C3) and (C4) for mode $m+2$ become

$$\begin{bmatrix} N_{11} & N_{12} \\ N_{21} & N_{22} \end{bmatrix}\begin{bmatrix} \alpha_1^{(m+2)} \\ \beta_1^{(m+2)} \end{bmatrix} = \begin{bmatrix} G_1 \\ G_2 \end{bmatrix}. \tag{C8}$$

The vectors $\boldsymbol{F}$ and $\boldsymbol{G}$ consist of the $O(\delta)$ solution which has undetermined coefficients α_0 and β_0. They also depend on known quantities, m, k_0, ω_0, ρ_2/ρ_1, S, and on the unknowns k_1 and ω_1.

https://doi.org/10.1017/jfm.2020.1157 Published online by Cambridge University Press

The matrices $\boldsymbol{M}$ and $\boldsymbol{N}$ on the left-hand side of (C7) and (C8) depend on m, ω_0, k_0, ρ_2/ρ_1, S. ($\boldsymbol{M}$, $\boldsymbol{N}$ and $\boldsymbol{F}$, $\boldsymbol{G}$ can be found in the Matlab supplementary material. We do not give them here because of their length.) The two linear systems are singular, i.e. their determinants are zero. The solvability condition requires that the vectors $\boldsymbol{F}$ and $\boldsymbol{G}$ lie in the image space of $\boldsymbol{M}$ and $\boldsymbol{N}$, i.e.

$$\left.\begin{aligned} M_{11}F_2 - M_{21}F_1 = 0, \\ N_{11}G_2 - N_{21}G_1 = 0. \end{aligned}\right\} \tag{C9}$$

Using the relations

$$\alpha_0^{(m)} = -\frac{\mathrm{i}\mathrm{J}_m(\eta_1)}{(\omega_0 - m)\mathrm{K}_m(k_0)}\beta_0^{(m)}, \quad \alpha_0^{(m+2)} = -\frac{\mathrm{i}\mathrm{J}_{m+2}(\eta_2)}{(\omega_0 - m - 2)\mathrm{K}_{m+2}(k_0)}\beta_0^{(m+2)}, \tag{C10a,b}$$

we substitute $\alpha_0^{(m)}$ and $\alpha_0^{(m+2)}$ into (C9) and convert it into a homogeneous linear system

$$\begin{bmatrix} D_{11} & D_{12} \\ D_{21} & D_{22} \end{bmatrix} \begin{bmatrix} \beta_0^{(m)} \\ \beta_0^{(m+2)} \end{bmatrix} = \boldsymbol{0}. \tag{C11}$$

For non-trivial $\beta_0^{(m)}$ and $\beta_0^{(m+2)}$, the resulting determinant equation

$$D_{11}D_{22} - D_{12}D_{21} = 0 \tag{C12}$$

leads to the dispersion relation for (k_1, ω_1). This is a quadratic equation for ω_1, where ω_1 is obtained from D_{11} and D_{22} via

$$D_{11} = \mu_1\omega_1 + \mu_2, \quad D_{22} = \mu_3\omega_1 + \mu_4. \tag{C13a,b}$$

The dispersion relation is hence

$$\mu_1\mu_3\omega_1^2 + (\mu_1\mu_4 + \mu_2\mu_3)\omega_1 + \mu_2\mu_4 - D_{12}D_{21} = 0. \tag{C14}$$

Expressions for μ_i and D_{12}, D_{21} are given in the supplementary material (Matlab scripts).

These quantities are functions of k_1 with m, ω_0, k_0, ρ_2/ρ_1 and S all given. The growth rate $\sigma_1 = |\mathrm{Im}(\omega_1)|$ has a maximum when $k_1 = 0$ where $\mu_2 = \mu_4 = 0$, giving

$$\sigma_{1max} = \sqrt{-\frac{D_{12}D_{21}}{\mu_1\mu_3}}. \tag{C15}$$

One half of the unstable bandwidth Δk_1 is calculated by finding the root k_1 of

$$(\mu_1\mu_4 + \mu_2\mu_3)^2 - 4\mu_1\mu_3(\mu_2\mu_4 - D_{12}D_{21}) = 0, \tag{C16}$$

and Δk_1 is calculated by solving a quadratic equation for the maximum root of k_1 in (C16).

References

Bayly, B.J. 1986 Three-dimensional instability of elliptical flow. *Phys. Rev. Lett.* **57**, 2160–2163.

Blanco-Rodriguez, F.J. & Le Dizès, S. 2016 Elliptic instability of a curved Batchelor vortex. *J. Fluid Mech.* **804**, 224–247.

Blanco-Rodriguez, F.J. & Le Dizès, S. 2017 Curvature instability of a curved Batchelor vortex. *J. Fluid Mech.* **814**, 397–415.

https://doi.org/10.1017/jfm.2020.1157 Published online by Cambridge University Press

CHANG, C. & LLEWELLYN SMITH, S.G. 2021 Density and surface tension effects on vortex ring stability. Part 1. Curvature instability. *J. Fluid Mech.* **913**, A14.

CROW, S.C. 1970 Stability theory for a pair of trailing vortices. *AIAA J.* **8**, 2172–2179.

DIXIT, H.N. & GOVINDARAJAN, R. 2011 Stability of a vortex in radial density stratification: role of wave interactions. *J. Fluid Mech.* **679**, 582–615.

ÉLOY, C. & LE DIZÈS, S. 2001 Stability of the Rankine vortex in a multipolar strain field. *Phys. Fluids* **13**, 660–676.

FUKUMOTO, Y. 2003 The three-dimensional instability of a strained vortex tube revisited. *J. Fluid Mech.* **493**, 287–318.

FUKUMOTO, Y. & HATTORI, Y. 2005 Curvature instability of a vortex ring. *J. Fluid Mech.* **526**, 77–115.

HATTORI, Y., BLANCO-RODRIGUEZ, F.J. & LE DIZÈS, S. 2019 Numerical stability analysis of a vortex ring with swirl. *J. Fluid Mech.* **878**, 5–36.

HATTORI, Y. & FUKUMOTO, Y. 2003 Short-wavelength stability analysis of thin vortex rings. *Phys. Fluids* **15**, 3151–3163.

JOLY, L., FONTANE, J. & CHASSAING, P. 2005 The Rayleigh–Taylor instability of two-dimensional high-density vortices. *J. Fluid Mech.* **537**, 415–431.

LEWEKE, T. & WILLIAMSON, C.H.K. 1998 Cooperative elliptic instability of a vortex pair. *J. Fluid Mech.* **360**, 85–119.

MOORE, D.W. & SAFFMAN, P.G. 1971 Structure of a line vortex in an imposed strain. In *Aircraft Wake Turbulence and its Detection* (ed. J.H. Olsen, A. Goldburg & M. Rogers), pp. 339–354. Plenum.

MOORE, D.W. & SAFFMAN, P.G. 1975 The instability of a straight vortex filament in a strain field. *Proc. R. Soc. Lond.* A **346**, 413–425.

SAUNDERS, P.M. 1973 The instability of a baroclinic vortex. *J. Phys. Oceanogr.* **3**, 61–65.

SIPP, D., FABRE, D., MICHELIN, S. & JACQUIN, L. 2005 Stability of a vortex with a heavy core. *J. Fluid Mech.* **526**, 67–76.

TSAI, C.Y. & WIDNALL, S.E. 1976 The stability of short waves on a straight vortex filament in a weak externally imposed strain field. *J. Fluid Mech.* **73**, 721–733.

WALEFFE, F. 1990 On the three-dimensional instability of strained vortices. *Phys. Fluids* A **2**, 76–80.

WIDNALL, S.E., BLISS, D.B. & TSAI, C.Y. 1974 The instability of short waves on a vortex ring. *J. Fluid Mech.* **66**, 35–47.

https://doi.org/10.1017/jfm.2020.1157 Published online by Cambridge University Press